Weld World (2016) 60:315–326
DOI 10.1007/s40194-015-0292-6

RESEARCH PAPER

Punching shear capacity of T-joint made of high-strength steel

T. Björk[1] · **A. Ahola**[1] · **T. Nykänen**[1]

Received: 16 June 2015 / Accepted: 28 December 2015 / Published online: 13 January 2016

Abstract Recently, the capacity of welded joints made of direct-quenched ultra-high-strength steel (with nominal yield strength of 960 MPa) has been increasingly investigated. However, less attention has been paid to joints subjected to shear loading. In this research, work the punching shear capacity of a plated structure was studied. The effects of cold forming and welding were also included in the study. The capacities based on analytical calculations were compared with experimental results and values obtained by FEA. The results matched each other quite well. The experimental results proved that if the heat input is moderate the welding alone has only a small effect on the punching shear capacity. However, the heat input together with cold forming seems to decrease the load carrying capacity more significantly.

Keywords (IIW Thesaurus) High-strength steels · Shear loading · Computation · GMA welding bend loading

1 Introduction

Welded connections can be categorized into load- and non-load carrying joints. Several capacity studies have been carried out recently by using load- and non-load-carrying joints made of ultra-high-strength steel (UHSS) [1–8]. These tests proved that the failures occurred in the base metal, in the weld, or in the softening HAZ of the joint, as illustrated in Fig. 1.

The location of the failure depends on the joint type (load- or non-load carrying), the throat thickness to plate thickness-ratio, and the cooling rate of the HAZ. The membranes tensile stress in the loading of the structural detail is the overarching feature for this research and the results. However, in T-joints the transverse shear stress can be the dominating load in the structural detail. The failure can occur in the transverse brace member (again in the base material or the HAZ), in the weld, or in the base plate. The loading of the base plate is a combination of shear and bending stresses and the proportion of each stress component is dependent on the joint dimensions. The larger the shear stress is in relation to the stresses due to the bending moment in the base plate, the more probabilistic the punching shear failure is the critical mode. In the case of direct-quenched (DQ) high-strength steels the softening can have a remarkable effect on the capacity of the joint. Although joints such as these are generally part of the structural details, no results about the capacity of joints made by DQ UHSS were available. Similar types of joints exist, e.g., in tubular structures, as illustrated in Fig. 2.

The reduced capacity of joints made of rectangular hollow section was in fact the purpose of this research. In this research work, the punching shear capacity of a T-joint made of plates was under investigation.

2 Goal

The goal of this research was to define the capacity and failure mechanics of T-joints made of DQ UHSS and subject them to punching shear failure. The main parameters for joints capacity were the load proportions of the joint, the heat input, and the degree of the (post-rolling) cold forming of the base plate.

Recommended for publication by Commission XV - Design, Analysis, and Fabrication of Welded Structures

✉ T. Björk
timo.bjork@lut.fi

[1] Laboratory of Steel Structures, Lappeenranta University of Technology, P.O. Box 20, FIN-53851 Lappeenranta, Finland

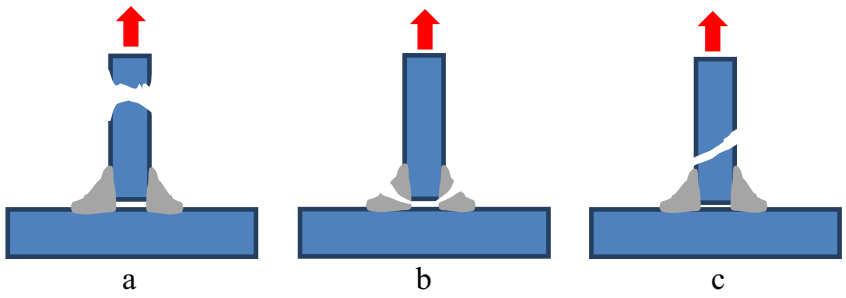

Fig. 1 Failure modes and places where the T-joint is subjected to the tensile load: **a** base material, **b** throat thickness, and **c** HAZ

3 Material

The investigated joints were fabricated of S960 QC steel using a GMAW-process. S960 QC steel is DQ UHSS with a nominal yield strength of 960 MPa. The filler material used was a slightly under-matching filler metal Böhler Union X96. The nominal chemical compositions and mechanical properties of the base and filler material are presented in Tables 1 and 2.

4 Experimental tests

4.1 Test specimens

Four simple T-joints were fabricated for investigation of the punching shear capacity of S960 QC steel. The type of the joint and dimensions are illustrated in Fig.3.

The failures of the welds and brace member (including also the HAZ) were not of interest and consequently were designed and fabricated to have more capacity than the base plate. The brace member was manufactured from two 8 mm plates, because a thicker brace member was not available in this material. However, the heat transform due to welding was calculated according to 8 mm plate thickness (Eq. 1), which decreased the cooling rate and thus increased the softening compared to single plate brace member with thickness of 16 mm. Consequently, the results will be on safe side if applied for thicker plate thicknesses made of this steel [5].

In order to include the softening effect of HAZ on the punching shear capacity of the joint, two different heat inputs were applied. The heat input together with the joint geometry defines the cooling rate, which together with the chemical compositions of the material determines the developing microstructure in the HAZ. If the heat input exceeds the value, and leads to a cooling time from a temperature of 800 to 500 °C which is longer than about $t_{8/5}=4$ s, the softening of S960 QC takes place and the strength of the material decreases. The critical cooling time can be estimated by the following equation [9, 10]

$$t_{8/5} = (4300-4.3T_0)\cdot 10^5 \left[\frac{\eta UI}{vt}\right]^2 \cdot \left[\left(\frac{1}{500-T_o}\right)^2 - \left(\frac{1}{800-T_o}\right)^2\right] F_2, \quad (1)$$

where

T_0 = initial plate temperature = 20 [°C]
η = thermal efficiency of the welding procedure = 0.85 for GMAW (process 135)
U = voltage [V]
I = current [A]
v = travel speed [mm/s]
t = plate thickness = 8 [mm]
F_2 = joint shape factor = 0.67 for T-joint

In order to avoid a weld failure, while still keeping the weld volume and thus the heat input moderate, a fully penetrated double bevel groove was prepared and welded either by one or two passes at each side as illustrated in Fig. 4. In all the joints, the throat thicknesses and leg lengths of the welds were larger than the thickness of the brace member.

In Table 3, the essential parameters of WPS (welding procedure specification) are presented. After each pass, the weld was cooled down to room temperature. The length of the weld is equal to the length of the specimen (=100 mm). The critical cooling time $t_{8/5}$ is estimated by the Eq. (1). However, this calculation method is just a rough estimation and the results are not absolute and should be confirmed by experimental measurements (e.g., thermocouples) but it works for comparison, because the joint geometry remains the same for all specimen.

Fig. 2 Punching shear failure of a tubular X-joint made of UHSS

Table 1 Chemical compositions of the used materials (nominal values, weight %)

Material code	C	Si	Mn	P	S	Al	Nb	Cu	Cr	Ni	Mo	CEV[a]
S960 QC	0.09	0.20	1.04	0.010	0.005	0.03	0.006	0.022	1.09	0.06	0.14	0.52
Union X96	0.10	0.81	1.94	0.015	0.011	–	–	0.08	0.52	2.28	0.53	0.79

[a] Carbon equivalent value CEV = C + Mn/6 + (Cr + Mo + V)/5 + (Ni + Cu)/15 [13]

Table 2 Mechanical properties of used materials (nominal values)

Material code	Yield strength $R_{p0.2}$ [MPa]	Tensile strength R_m [MPa]	Elongation A [%]	Charpy V impact energy temperature	
				CV [J]	T [°C]
S960 QC	960	1000	11	65	−65
Union X96	930	980	14	47	−50

In test LF4, the effect of cold forming was included. Therefore, the base plate was bent out of the plane to an angle of 65°, as illustrated in Fig. 5, and afterwards straightened back to the original shape and welded to the brace member. This is far from an exact simulation of the deformation process in the corner of the rectangular hollow section. However, the pre-bending involves the effect of cold forming on the general behavior of the welded joint.

4.2 Test set up

Two types of test set up were used: a pure punching shear loading (denoted by Q) and a combination with a bending moment (denoted by $Q+M$) as illustrated in Fig. 6.

The main parameters for the test set up can be seen in Table 4. The specimens are categorized according to heat inputs (low, middle, and great), with reference to the last two passes of the joint. The joint geometry is the same for each test.

The laboratory set up is illustrated in Fig. 7. The load was applied by a pin end fixing. The test with specimen LF1 was unsuccessful, because the capacity of the clamps was too low. The load and displacement of the loading point were measured. The displacement also included the flexibility of the loading rig, which is negligibly small compared to the specimen's flexibility. The tests were carried out at room temperature.

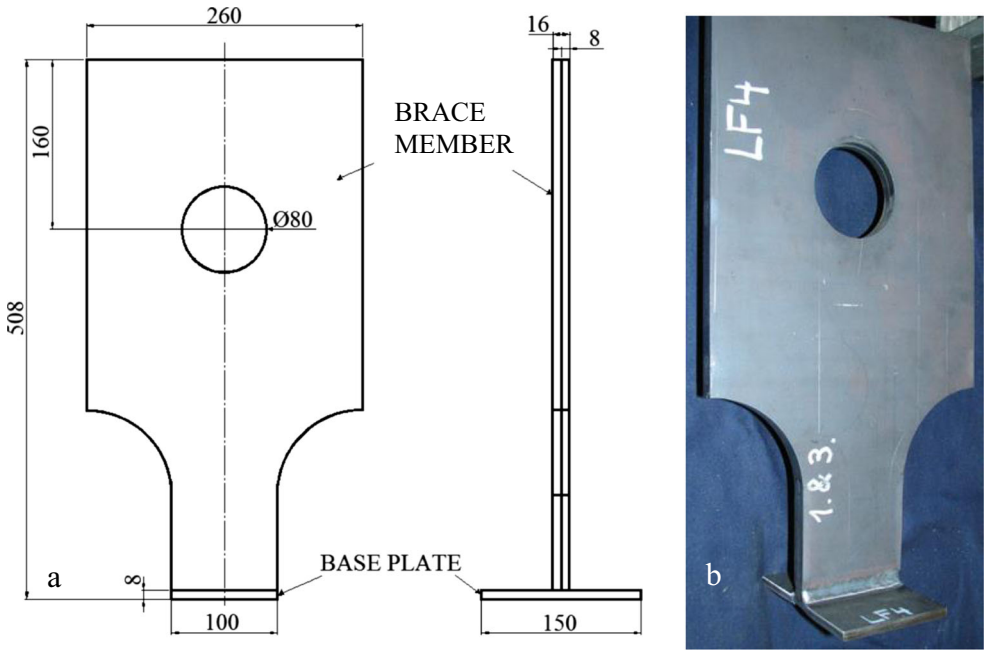

Fig. 3 Test specimen: **a** dimensions and **b** a fabricated example

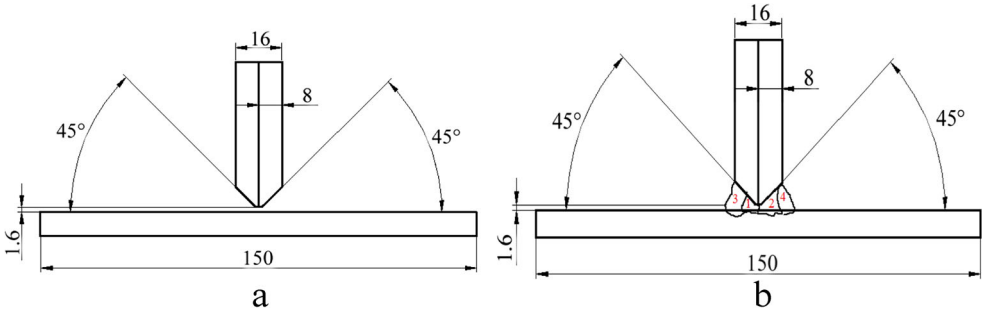

Fig. 4 Preparation of the joint: **a** double preparation and **b** sequence of welds

4.3 Results

The results from the laboratory test can be seen in Figs. 8 and 9. The ultimate capacity, total displacement, and plastic deformation with reference to the maximum load capacity of the joint are plotted in Table 5. The definition principle of these values from the F-δ-diagrams is illustrated in Figs. 8 and 9.

The failure mode of all specimen was ductile with some amount of plastic deformation. Of course the test with ligament e (LF5) was more flexible and amount of plastic deformation was larger but capacity was lower compared to the tests with pure shear loading.

The typical failure modes are illustrated in Fig. 10. Figure 10a illustrates the failure of test specimens LF2-4 and 10b FL5, respectively. The typical punching shear failure was occurred in all specimens but only in the case of pure shear loading the step due to shear deformation was clearly seen before rupture. The experimental results are discussed more detailed in Chapter 6.

5 Analyses

5.1 Analytical approach

The punching shear failure of a symmetric T-joint is illustrated in Fig. 11. The length of the joint is $L = 100$ mm and the yield strength of the bottom plate is f_y.

The capacity can be calculated based on the lower or upper limit state [11]. The lower limit capacity, based on starting yielding in the middle of the base plate and von Mises yield hypothesis, is

$$F_{y,\mathrm{low}} = 2Q = \frac{4Ltf_y}{3\sqrt{3}} \tag{2}$$

The upper yield limit is obtained by assuming constant shear stress over the plate thickness

$$F_{y,\mathrm{upp}} = \frac{2Ltf_y}{\sqrt{3}} \tag{3}$$

Table 3 Welding parameters

ID	Number of passes	Current I [A]	Voltage U [V]	Travel speed v [mm/s]	Wire feed rate [m/min]	Heat input Q [kJ/mm]	Cooling time $t_{8/5}$ [s]
LF2	1	247	27.2	3.2	10.7	1.67	37.89
	2	240	27.2	3.4	10.7	1.51	31.69
LF3	1	217	24.8	6.3	9.9	0.69	6.27
	2	218	24.8	6.3	9.9	0.69	6.33
	3	240	27.2	4.2	10.7	1.25	20.76
	4	242	27.2	4.2	10.7	1.26	21.11
LF4	1	215	24.8	5.9	9.9	0.73	7.02
	2	214	24.8	5.9	9.9	0.72	6.96
	3	244	27.2	4.2	10.7	1.27	21.46
	4	238	27.2	4.2	10.7	1.24	20.42
LF5	1	210	24.8	5.9	9.9	0.71	6.70
	2	215	24.8	5.6	9.9	0.77	7.79
	3	252	27.2	4.5	10.7	1.21	19.94
	4	250	27.2	5.0	10.7	1.09	15.90

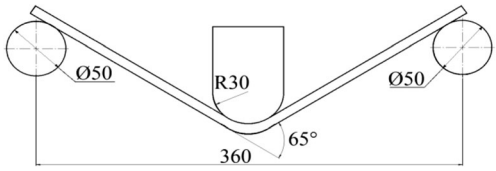

Fig. 5 Pre-bending of the base plate

The similar upper and lower limits can also be assumed based on the ultimate tensile strength f_u of the material. Based on the nominal material properties shown in Table 3, the summary about these calculations are presented in Table 6. The levels of theoretical capacities ($F_{y,\mathrm{low}}$, $F_{y,\mathrm{upp}}$,$F_{u,\mathrm{low}}$, and $F_{u,upp}$) are indicated in Fig. 8.

In the test, the LF5, the clamps are at a distance of $e=16$ mm from the weld toe as illustrated in Fig. 12.

The shear and bending stresses have an interaction on the intersection of high $2z_0$ in the middle of the base plate. If the section is assumed to be in a fully plastic condition then the material plasticity follows the von Mises yield criterion, and based on Fig. 13 the following is obtained:

$$d\sigma dz = -d\tau dx \tag{4}$$

$$d\tau = -\frac{d\sigma}{dx}dz = -\frac{dM}{Idx}zdz = -\frac{Q}{I}zdz \tag{5}$$

$$\tau = \int_z -\frac{Q}{I}zdz = -\frac{Q}{2I}z^2 + \tau_0 \tag{6}$$

$$\begin{aligned} \tau_{z=z_0} = 0 \Rightarrow \tau_0 &= \frac{Q}{2I}z_0^2 \\ \tau &= \frac{Q}{2I}\left(z_0^2 - z^2\right) \end{aligned} \tag{7}$$

Where

$$z_0 = \frac{3\sqrt{3}Q}{4Lf_y} \text{ and } I = \frac{2Lz_0^3}{3}$$

For the inner section of the base plate, the bending stress σ is available

$$\sigma = \sqrt{f_y^2 - 3\tau^2} = \sqrt{f_y^2 - 3\left[\frac{Q}{2I}\left(z_0^2 - z^2\right)\right]^2} \tag{8}$$

The stress is in equilibrium with elastic moment M_E acting in the inner section ($2z_0$) of critical ligament

$$\begin{aligned} M_E &= 2\int_0^{z_0} \sigma L z dz = 2L\int_0^{z_0} \sqrt{f_y^2 - 3\left[\frac{Q}{2I}\left(z_0^2 - z^2\right)\right]^2}\, z dz \\ &= 2\frac{f_y L}{z_0^2}\int_0^{z_0} \sqrt{2z_0^2 - z^2}\, z^2 dz \end{aligned} \tag{9}$$

If we mark the $z = sz_0$ and $dz = z_0 ds$

$$\begin{aligned} M_E &= 2f_y L z_0^2 \int_0^1 \sqrt{2-s^2}\, s^2 ds \\ M_E &= \frac{1}{2}f_y L_{00}^{21}\left[2\arcsin\left(\frac{s}{\sqrt{2}}\right) - s\sqrt{-(s^2-2)^3} + s\sqrt{2-s^2}\right]^0 \\ &\quad + M_{E,0} = \frac{\pi}{4}f_y L z_0^2, \quad M_{E,0} = 0 \end{aligned} \tag{10}$$

The moment capacity of the plate M is consisting of plastic part M_{pl} acting in outer section and elastic part M_E acting in inner section of plate as illustrated in Fig. 12

$$\begin{aligned} M &= M_{pl} + M_E = f_y L\left[\left(\frac{t^2}{4} - z_0^2\right) + \frac{\pi}{4}z_0^2\right] \\ &= f_y L\left[\frac{t^2}{4} - \left(1 - \frac{\pi}{4}\right)z_0^2\right] \end{aligned} \tag{11}$$

The capacity of the joint is

$$F = 2Q = \frac{4M}{e} = \frac{4f_y L}{e}\left[\frac{t^2}{4} - \left(1 - \frac{\pi}{4}\right)\frac{27Q^2}{16L^2 f_y^2}\right] \tag{12}$$

Now the shear force Q can be solved

$$\left(1 - \frac{\pi}{4}\right)\frac{27Q^2}{16}Q^2 - \frac{f_y L e}{2}Q + \frac{t^2}{4}L^2 f_y^2 = 0 \tag{13}$$

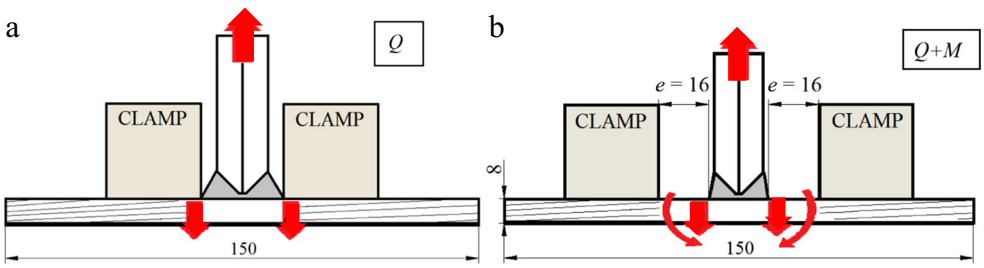

Fig. 6 Test set up: **a** a pure punching shear and **b** a combination with a bending moment

Table 4 Test matrix

Specimen ID	Pre-bending of base plate	Heat input (one or two passes)	Loading
LF2	No	Great	Q
LF3	No	Low	Q
LF4	Yes	Low	Q
LF5	No	Middle	Q + M

By marking

$$a = -\frac{8}{27\left(1-\frac{\pi}{4}\right)} = -1.3807$$

$$Q = \frac{af_yLe}{2}\left(1-\sqrt{1-\frac{2t^2}{ae^2}}\right)$$

$$Q = \frac{-1.3807 \cdot 960 \cdot 100 \cdot 16}{2}\left(1-\sqrt{1+\frac{2 \cdot 8^2}{1.3807 \cdot 16^2}}\right) = 177\,\text{kN}$$

$$F_y = 2Q = 354\ \text{kN} \tag{14}$$

The joint capacity calculated according to the ultimate tensile strength $f_u = 1000$ MPa is

$$F_u = 368\ \text{kN}$$

The shear stress at the limit state can be assumed to have different simplified distributions as illustrated in Fig. 14.

If the moment capacity of the middle part is simply omitted as illustrated in Fig. 14a, the moment capacity of the plastic hinge is

$$M = M_{pl} = f_yL\left(\frac{t^2}{4}-z_0^2\right) \tag{15}$$

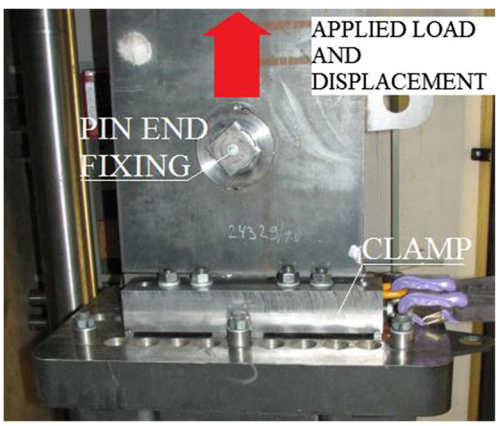

Fig. 7 Laboratory test arrangement

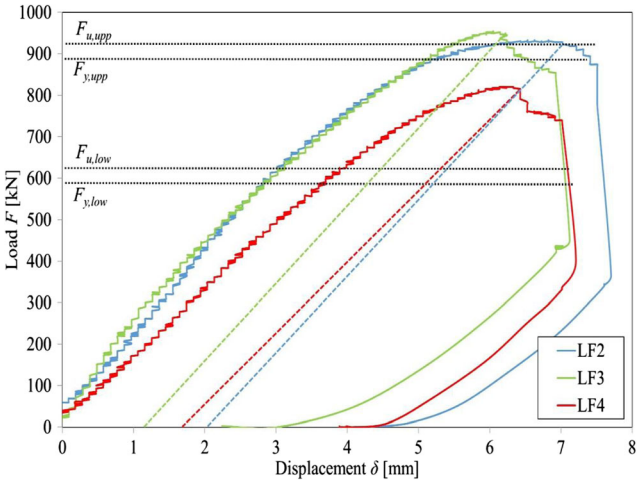

Fig. 8 Results of test specimens LF2, 3, and 4

where

$$z_0 = \frac{3\sqrt{3}Q}{4Lf_y}$$

$$M = f_yL\left(\frac{t^2}{4}-\frac{27Q^2}{16L^2f_y^2}\right) = \frac{Qe}{2} \tag{16}$$

Then the shear force capacity can be defined as

$$Q^2+\frac{8Lef_y}{27}Q-\frac{4\left(Ltf_y\right)^2}{27} = 0 \tag{17}$$

$$Q = \frac{2Lf_y}{27}\left[\sqrt{4e^2+27t^2}-2e\right]$$

$$= \frac{2 \cdot 100 \cdot 960}{27}\left(\sqrt{4 \cdot 16^2+27 \cdot 8^2}-2 \cdot 16\right) = 145\ \text{kN} \tag{18}$$

The joint capacity is

$$F_y = 2Q = 291\ \text{kN}$$

Table 5 Capacities from the laboratory tests

Specimen ID	Ultimate capacity F_u [kN]	Total displacement δ_u [mm]	Plastic deformation δ_p [mm]
LF2	932	7	2.0
LF3	953	6.3	1.2
LF4	820	6.5	1.6
LF5	416	7.5	4.5

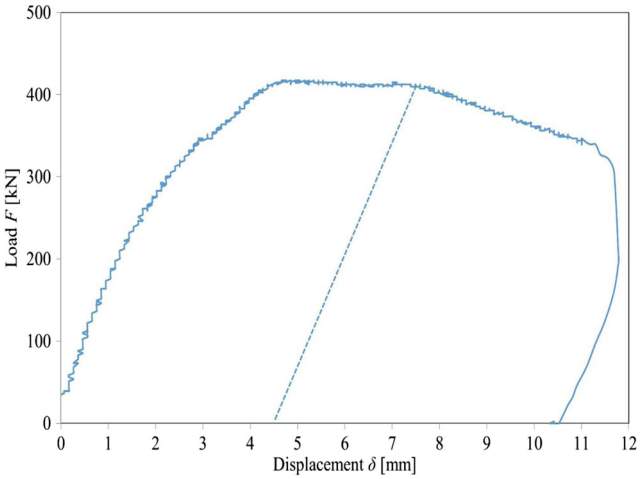

Fig. 9 Results of test specimens LF5

If the shear stress is assumed to be uniformly distributed over the length $2z_o$ as illustrated in Fig. 14b,

$$z_0 = \frac{\sqrt{3}Q}{2Lf_y}$$

then the joint capacity can be calculated from the moment capacity

$$M = f_y L\left(\frac{t^2}{4} - \frac{3Q^2}{4L^2 f_y^2}\right) = \frac{Qe}{2} \tag{19}$$

$$Q = \frac{Lf_y}{3}\left[\sqrt{e^2 + 3t^2} - e\right]$$
$$= \left[\frac{100{\cdot}960}{3}\sqrt{16^2 + 3{\cdot}8^2} - 16\right] = 165 \text{ kN} \tag{20}$$

$F_y = 2Q = 330$ kN.

If the shear stress is assumed to be uniformly distributed over the plate thickness t as illustrated in Fig. 14c, and the von Mises yield criterion is applied, the capacities are

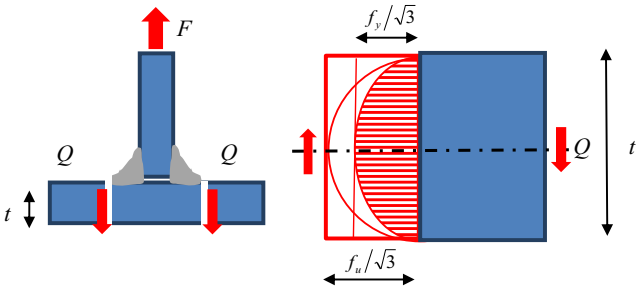

Fig. 11 The punching shear failure of a T-joint

$$M = \frac{Lt^2}{4}\sqrt{f_y^2 - 3\tau^2} = \frac{Qe}{2} \tag{21}$$

$$Q = \frac{Lf_y t^2}{\sqrt{4e^2 + 3t^2}} = \frac{100{\cdot}960{\cdot}8^2}{\sqrt{4{\cdot}16^2 + 3{\cdot}8^2}} = 176 \text{ kN} \tag{22}$$

$F_y = 2Q = 352$ kN

5.2 Finite element analysis

Non-linear finite element calculations were carried out in order to compare the behavior with the theoretical models. Parabolic plain strain elements were used and the FE-model of the critical join area with mesh is seen in Fig. 15a. The softening area near the weld toe was considered by reducing the yield and ultimate strength (σ_{soft}) according to the measured hardness (H_{soft}) distribution and comparing them to the values of base material (σ_{bm}, H_{bm}) and using simple Cahoon relationship [12].

$$\sigma_{soft} = \frac{H_{soft}}{H_{bm}}\sigma_{bm} \tag{23}$$

The reduced material area can be seen in Fig. 15a (red area), the used material models in Fig. 15b and the hardness distributions in Fig. 19. The true stress-strain curves were created based on nominal material values presented in Table 2.

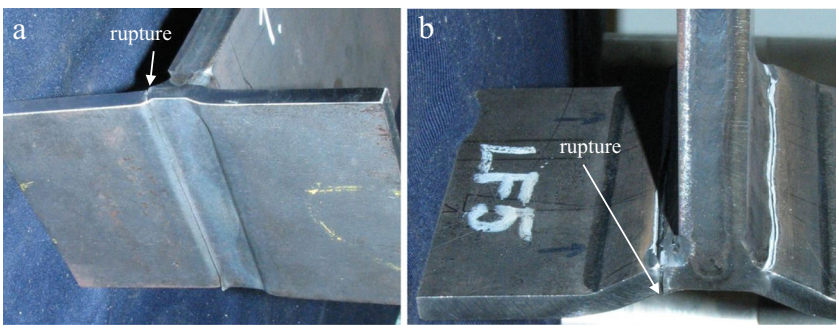

Fig. 10 Failure modes for specimens: **a** LF2-4 and **b** LF5

Table 6 Theoretical capacities of the T-joint

Specimen ID	Yield strength capacity		Ultimate capacity	
	$F_{y,\mathrm{low}}$ [kN]	$F_{y,\mathrm{upp}}$ [kN]	$F_{u,\mathrm{low}}$ [kN]	$F_{u,\mathrm{upp}}$ [kN]
LF2, 3, and 4	591	887	619	924

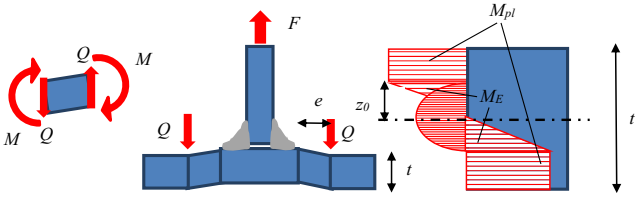

Fig. 12 Q + M interaction as a failure mechanism of the base plate

The calculations included two different boundaries ($e=0$ and $e=2\,t$) referring to the experimental tests. The calculations were carried out by an NX-NASTRAN program and the F-δ-curves can be seen in Fig. 16. The calculations obtain the ultimate capacities $F_{u,\mathrm{FEM}}=1040$ kN for $e=0$ and $F_{u,\mathrm{FEM}}=480$ kN for $e=16$ mm, respectively. The results are discussed more detailed in Chapter 6.

In Fig. 17, the normal and shear stress distribution over the plate thickness can be seen at the weld toe in the cases $e=0$ and $e=2\,t$. The stresses are referring the limit load of the joints.

In Fig. 18, the plastic strain distribution at the weld toe is seen, when the load of the joint is approaching its limit state.

6 Discussion

In Fig. 19, the hardness distributions at the weld toe can be seen. The horizontal distribution is representing values measured at distance of 1 mm from plate surface and the vertical values the (white) line fixed at weld toe. In Fig. 19a, b, the effect of the larger heat input (LF2) and in the Fig. 19c, d the lower (LF3) can be seen, respectively. There exist some differences in hardness distribution depending on number of passes and also between the first and second run. The hardness and thus ultimate strength varies considerably along the fracture path, which is the most interesting area. There is a hard zone behind the fusion line and then an approximately 2-mm wide softened zone next to the hardened zone.

The material model for FEA was fixed by means of the measured hardness distribution as shown in Fig. 15. The liner correlation in Eq. 23 is based on the fact, that for this material the strain hardening will not compensate the lost strength due to softening [5]. The typical microstructures of different weld zones for a joint made of S960 QC can be seen in Fig. 20.

The microstructure of the weld is martensitic but behind the fusion line (fl) it is upper bainite and martensite with a coarse grain size. The HAZ1 has a partly austenitic structure and HAZ2 a ferritic microstructure with a small grain size. Except in the weld, the fracture passes through all the zones and also the base material, which is banite-martensite with a very small grain size. The different microstructures are the reason for the different hardness- and strength zones over the thickness of the critical sections. The punching shear capacity is dependent on the displacement-controlled failure process over the whole thickness of the base plate. Consequently, the capacity is dependent both on the strength and the ductility of the zones. The ruptured surfaces of the base plate at the weld toes are presented in Fig. 21. The upper surface illustrated is the side of the weld.

The differences in heat input and cooling time does not cause any remarkable distinguishing features either on the fractured surfaces or on the load carrying capacity. Unexpectedly, the joint with the larger heat input had a better ultimate deformation capacity. The cold forming decreased the load carrying capacity of the joint (14 %). In addition, the stiffness of the joint seems to be lower in reference to the residual stresses equal to the yield strength of the base plate.

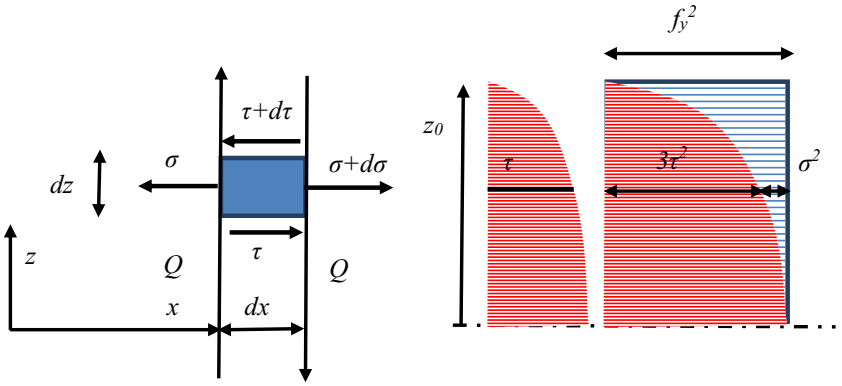

Fig. 13 Stress components on the middle part of the plate under Q + M interaction

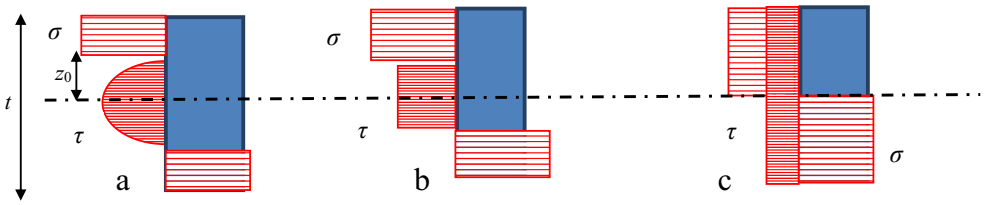

Fig. 14 Shear stress distributions: **a** parabolic, **b** uniformly, and **c** uniformly over the thickness

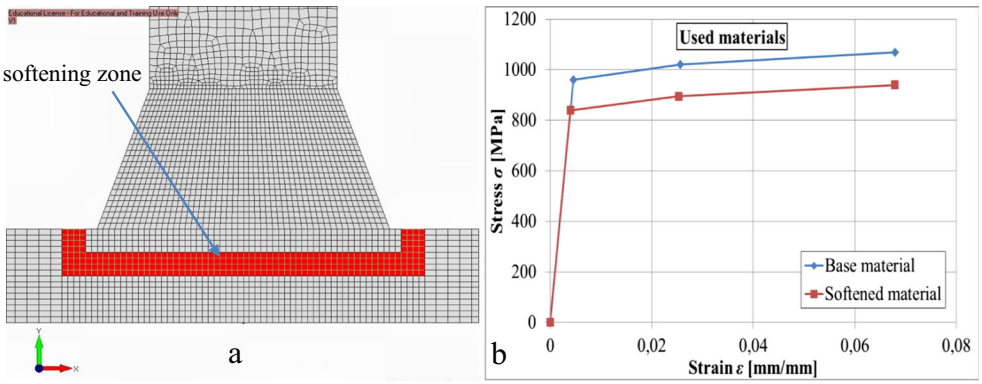

Fig. 15 FEA model: **a** used mesh and material models

This can be the case, because the degree of cold forming was high due to the pre-bending of the palate before welding.

The shear capacity of the joint can be defined as a function of the ligament relative length *e/t*. The capacity of the base plate based only on the bending moment is

$$Q = \frac{\sqrt{3}}{2}\frac{e}{t}\frac{Lf_y t}{\sqrt{3}} = q_o \frac{Lf_y t}{\sqrt{3}} = q_o Q_{pl} \tag{24}$$

The capacities based on different shear stress distributions at the limit states, as illustrated in Figs. 13 and 14, can be presented by the following equations

$$Q_{13} = 1.196\left[\sqrt{\frac{e^2}{t^2} + 1.4486} - \frac{e}{t}\right]\frac{Lf_y}{\sqrt{3}} = q_{13}Q_{pl} \tag{25}$$

$$Q_{14a} = \frac{2}{9\sqrt{3}}\left[\sqrt{\frac{4e^2}{t^2} + 27} - \frac{2e}{t}\right]\frac{Lf_y}{\sqrt{3}} = q_{14a}Q_{pl} \tag{26}$$

$$Q_{14b} = \frac{1}{\sqrt{3}}\left[\sqrt{\frac{e^2}{t^2} + 3} - \frac{e}{t}\right]\frac{Lf_y}{\sqrt{3}} = q_{14b}Q_{pl} \tag{27}$$

$$Q_{14c} = \frac{1}{\sqrt{\frac{4e^2}{3t^2} + 1}}\frac{Lf_y t}{\sqrt{3}} = q_{14c}Q_{pl} \tag{28}$$

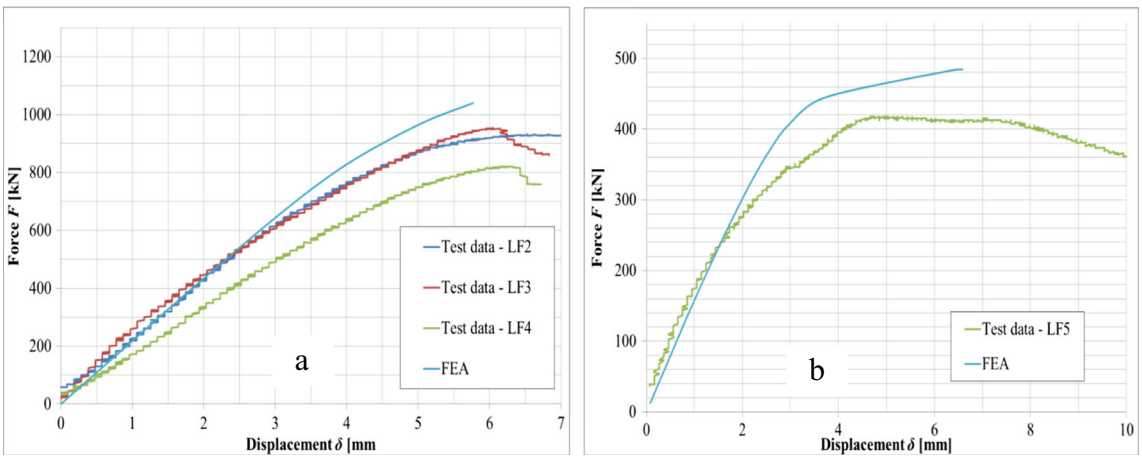

Fig. 16 *F*-*δ*-curves defined by FEA (test results for comparison): **a** $e = 0$ and **b** $e = 16$ mm

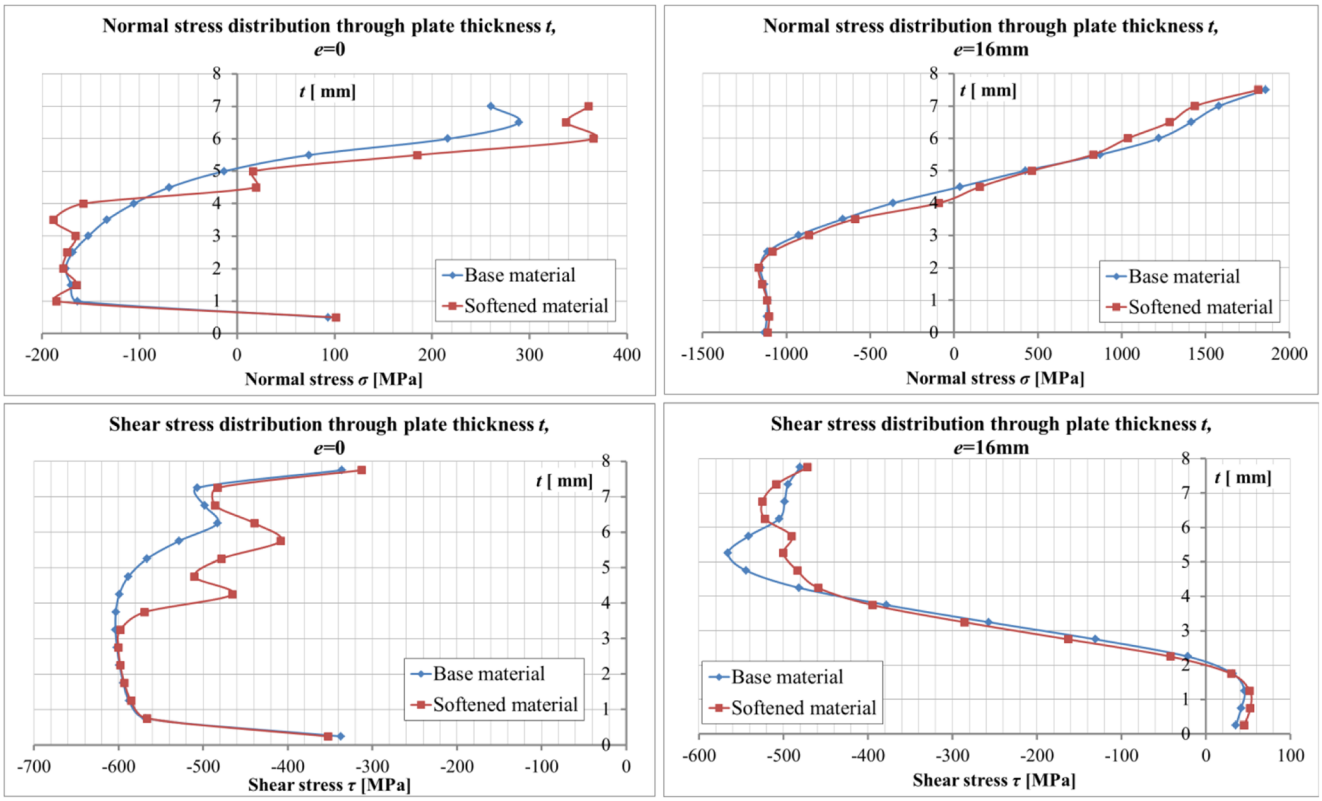

Fig. 17 Stress distribution at the joints

The functions are presented in Fig. 22. The horizontal difference between the curve q_0 and others shows the reduction due to shear stress for each *e/t* ratio.

All the theoretical models predicted nearly the same capacity, when the *e/t* ratio exceeds the value 2. The shear force effect on the joint capacity below this value is important to consider. The theoretical models can be remarkably distinguished when the punching shear mechanism dominates (*e/t* = 0). The new capacity model (Fig. 13) presented overestimates the punching shear capacity. The simple assumption about uniform shear stress distribution over the plate thickness (Fig. 14c) obtains the best agreement with the experimental results.

The experimental capacities and the results from FEA are also plotted in Fig. 17. The comparison is carried out by using the ultimate nominal strength instead of the yield strength, because the ultimate capacity can be defined more exactly from the experimental results than the yield capacity. The experimental *q* values are 1.01, 1.03, 0.89, and 0.45 for joints LF2, 3, and 5, respectively. The values from FEA overestimated the joint capacity compared to the experimental and analytical results. The used assumption about the

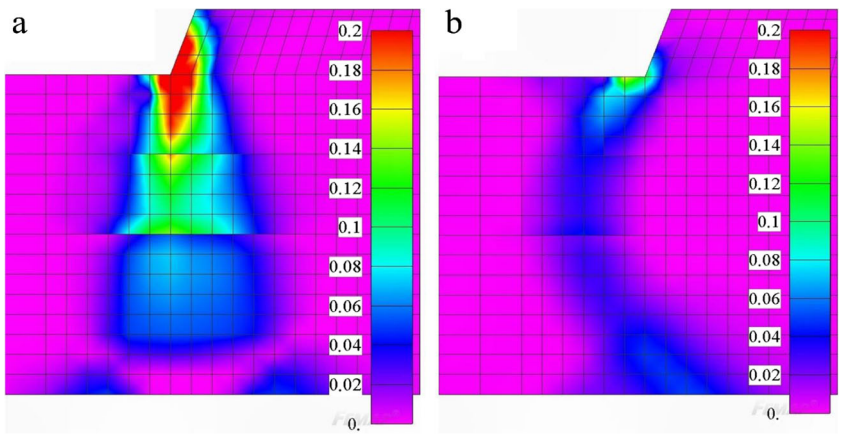

Fig. 18 Strain distribution at the joint: **a** *e* = 0 and **b** *e* = 16 mm

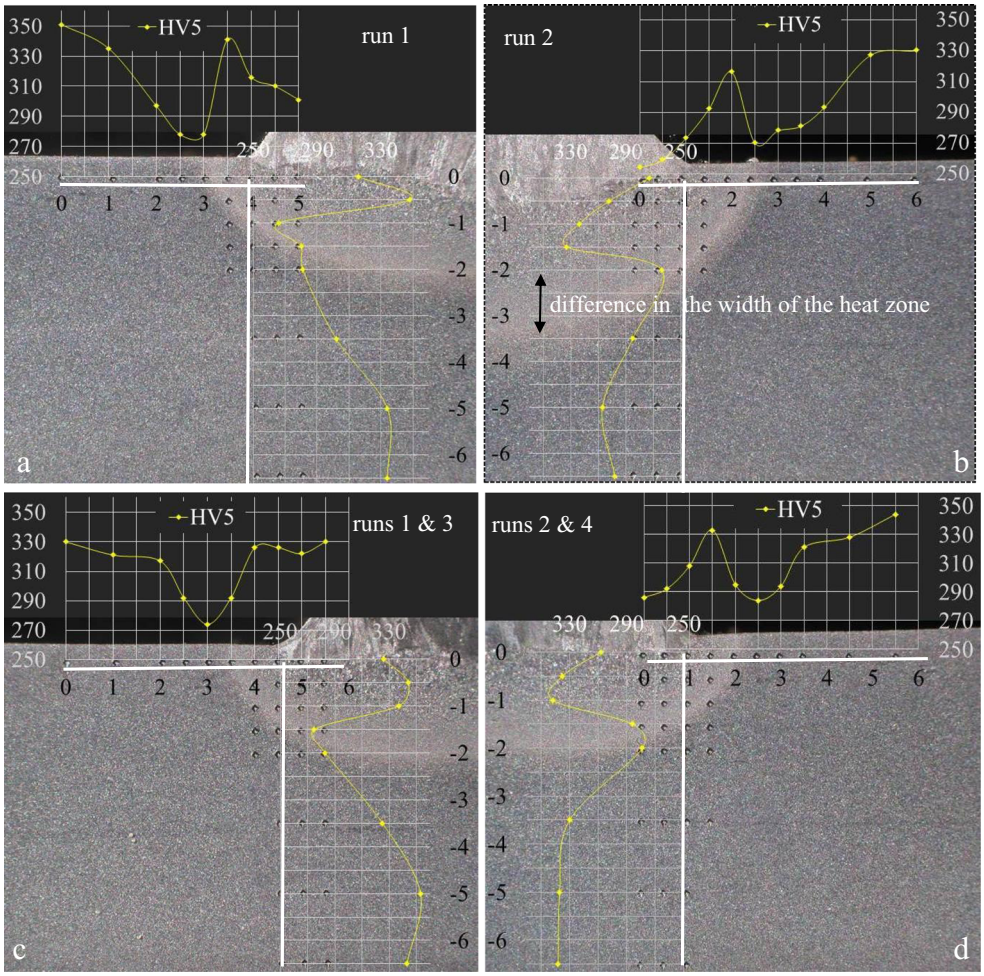

Fig. 19 Hardness distributions: **a**, **b** one pass and higher heat input and **c**, **d** two passes and lower heat input

softening area and its impact on the strength properties seems to have little effect on the joint capacity. One reason for the differences in the results can be due to the use of the simplified material model and the use of a 2D instead of a 3D model. The plain strain elements used overestimate the capacity of the end sections of the joints. The other reason for the differences is the deformations of the clamps, which were ignored in FEA. The considering of the clamps with the fixing bolts would obtain more flexibility and less ultimate capacity for the joint in FEA and consequently improved the agreement of results. However, a closer comparison would require the measuring of clamp deformations, which was ignored in this research.

This study did not obtain any good reason for the reduced punching shear capacity of RHS-joint. There must be some other phenomena for this case, such as potential aging. The effects were not activated in the case of plated structures, even when it was subjected to cold forming and welding, which could render the joint prone to aging. The degree of cold forming in the corner of RHS-joint is higher compared to this T-joint, but the failure did not occurred in the corner of the

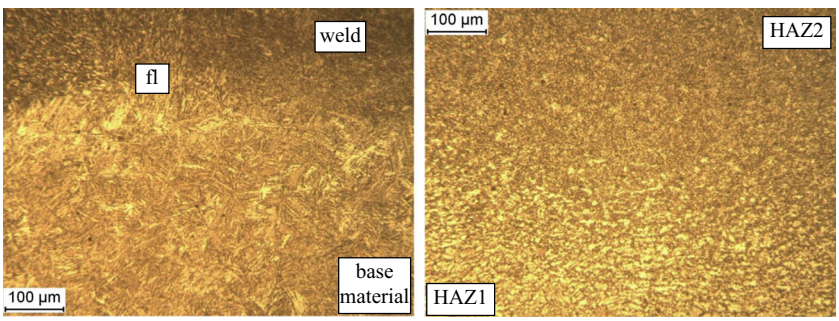

Fig. 20 Microstructures: **a** both sides of the fusion line (fl) and **b** in HAZ

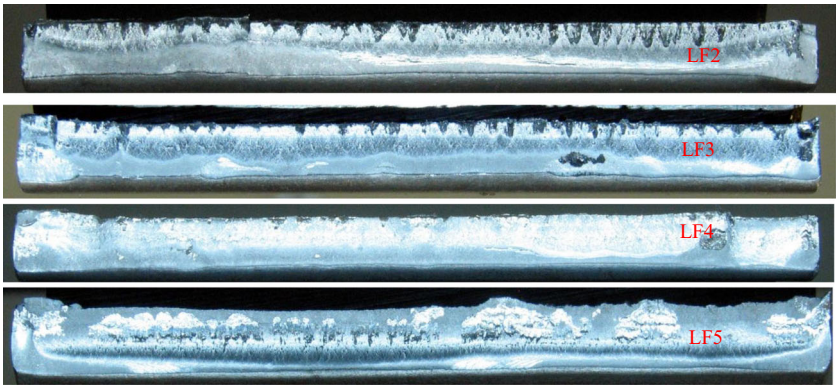

Fig. 21 The failure surfaces of the base plates

RHS-joint (see Fig. 2). Of course in the RHS-joint the shear force is doubled at the critical weld toe compared to the load in the T-joint, but this was considered when the amount of reduction was calculated.

7 Conclusions

Based on several experimental tests and theoretical calculations, the following conclusions can be drawn:

- The reduced capacity due to punching shear failure of tubular joints was not recognized in plated joints
- The joint capacity was good in terms of load and deformation (the latter is always quite limited in punching shear failure)
- Although the greater heat input caused a slightly larger softening area near the weld toe, it did not make any significant difference in the joint capacity
- The experimental results corresponded very well with the theoretical values without any reduction factors, which are sometimes required due to the high steel grade
- The simple assumption about uniform shear stress distribution over the plate thickness (Fig. 14c) obtained the best agreement with the experimental and theoretical values

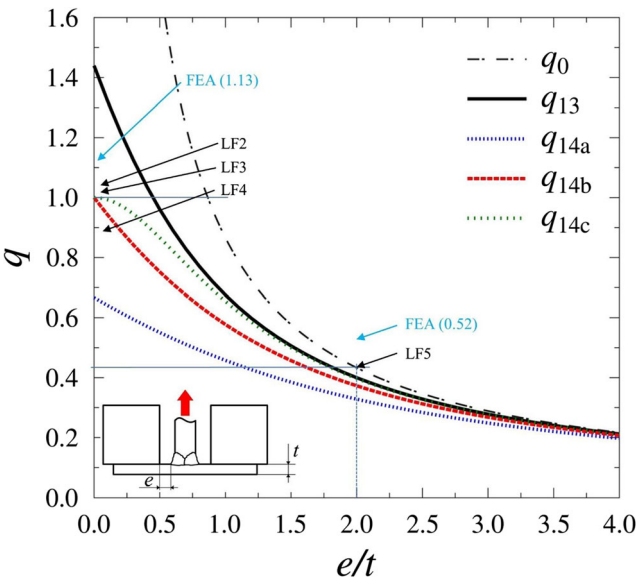

Fig. 22 Shear capacity of the plastic hinge depending on the *e/t* ratio

Acknowledgments The authors wish to thank SSAB Oy for supplying the materials and TEKES/FIMECC for providing the funding for this project, which is part of the MANU program.

References

1. Hölbling W, Muller G, Saal H (2005) Tragverhalten von Kehlnahtverbindungen von höherfesten Feinkornbaustählen. Stahlbau 74(1):1–8. doi:10.1002/stab.200490250
2. Kuhlmann U, Günther H-P, Rasche C (2008) High-strength steel fillet welded connections. Steel Constr Des Res 1(1):77–84. doi:10.1002/stco.200890013
3. Herion S, Fleicher O (2012) Reduction of weld sizes. CIDECT Report 5BY-5/11, Final Report
4. Knurshid M, Barzom Z, Mumtaz N (2012) Ultimate strength and failure modes for fillet welds in high strength steels. Mater Des 40: 36–42. doi:10.1016/j.matdes.2012.03.048
5. Björk T, Toivonen J, Nykänen T (2012) Capacity of fillet welded joints made of ultra-high-strength steel. Welding in the World 56(3): 71–84
6. Penttilä T (2012) Static strength design of fillet welds with conventional methods and new improved design methods based on different boundary conditions (in Finnish). In proceedings of the 11th Finnish Mechanics Days
7. Valkonen I (2014) Estimation of limit load capacity of structural steel with yield strength 960 MPa. Welding in the Word 58(6):839–852
8. Björk T, Penttilä T, Nykänen T (2014) Rotation capacity of fillet weld joints made of high-strength steel. Welding in the Word 58(6):853–863
9. EN 1011-2 (2001) Welding—recommendations for welding of metallic materials—Part 2: arc welding of ferritic steels
10. Balogh A, Kirk S, Görbe Z (1999) Role of cooling time when steels to be welded require controlled heat input. GÉP, L. évfolyam, pp 44-50
11. EN 1993-1-1 (2005) Eurocode 3: design of steel structures—Part 1-1: generals rules for buildings
12. Pavlina EJ, Tyne CJV (2008) Correlation of yield strength and ultimate strength with hardness of steels. J Mater Eng Perform 17(6):888–893. doi:10.1007/s11665-008-9225-5
13. Ginzburg V B, Ballas R (2000) Flat rolling fundamentals, CRC Press, pp 141–142